Extraction of Ocean Wave Spectra From Simulated Noisy Bistatic High-Frequency Radar Data

Jianjun Zhang and Eric W. Gill, *Senior Member, IEEE*

***Abstract*—An algorithm is developed for the inversion of bistatic high-frequency (HF) radar sea echo to give the nondirectional wave spectrum. The bistatic HF radar second-order cross section of patch scattering, consisting of a combination of four Fredholm-type integral equations, contains a nonlinear product of ocean wave directional spectrum factors. The energy inside the first-order cross section is used to normalize this integrand. The unknown ocean wave spectrum is represented by a truncated Fourier series. The integral equation is then converted to a matrix equation and a singular value decomposition (SVD) method is invoked to pseudoinvert the kernel matrix. The new algorithm is verified with simulated radar Doppler spectrum for varying water depths, wind velocities, and radar operating frequencies. To make the simulation more realistic, zero-mean Gaussian noise from external sources is also taken into account.**

***Index Terms*—Bistatic cross section, high-frequency (HF) radar, inversion algorithm, waveheight spectra.**

I. Introduction

HIGH-FREQUENCY (HF) ground-wave radar has the potential for sensing ocean surface parameters to ranges exceeding 200 km from the coastline. At HF, the transmitted signal, which is guided by a good conducting medium like ocean water, travels along the earth's curvature, reaches far beyond the line-of-sight horizon, and couples strongly with the ocean surface. The returning signals contain a large amount of information on ocean currents, waves, and winds. The speed of the ocean waves generally causes Doppler shifts on the incident radar carrier frequency. Typically, the resulting Doppler radar spectra are characterized by two significant "first-order" peaks (Bragg peaks [1]) surrounded by a higher order continuum (see Fig. 1). As is well known now, this continuum contains information on the ocean wave regime. The procedure of extracting this information from the Doppler spectrum is referred to here as the inverse analysis.

Historically, HF radar has been operated as a remote sensor in monostatic mode (transmitter and receiver are essentially colocated). Recently, bistatic operation (transmitter and receiver are widely separated) has been considered and, consequently, a need has arisen for bistatic inversion schemes. Compared with a monostatic configuration, a bistatic configuration possesses some advantages in practical utilization. For instance, it is possible to use one full monostatic radar system in combination with a remote receiver, rather than two complete, widely separated monostatic radar systems, to obtain wave directional information.

The derivation of the HF radar cross section for the ocean began initially with Barrick [2], [3]. Barrick and Lipa [4] further derived a set of expressions to account for shallow water. Subsequently, based upon Walsh's generalized-function approach [5], Srivastava [6] developed the first- and second-order monostatic cross sections in an alternative way. Walsh *et al.* [7] carried a similar analysis to third-order cross section. Assumptions are made of grazing incidence and vertical polarization of the radar wave. The first inverse analysis model was developed by Barrick [8]. Lipa [9] reduced Barrick's second-order cross section to a linear equation by means of a stabilization technique using a Phillips equilibrium spectrum [10]. A detailed theoretical analysis was presented by Lipa and Barrick [11]. Their work was extended by Wyatt [12] and Wyatt *et al.* [13] to derive ocean wave information from a greater range of Doppler frequencies. Lipa and Barrick [14] presented another extension to include an ocean region of arbitrary depth. Howell and Walsh [15] and Gill and Walsh [16] produced algorithms for the inverse analysis by means of singular value decomposition (SVD) routines for narrowbeam and widebeam cases, respectively.

Among some of the most recent progress in the development of HF radar cross sections of the ocean surface, Gill and Walsh [17] have presented bistatic first- and second-order radar cross sections using the generalized-function approach [5]. The locations of the first-order peaks are shown to be at Doppler radian frequencies of $\omega_B = \pm\sqrt{2gk_0\cos(\phi_0)}$ if deep water is assumed. Here, g is the acceleration due to gravity, k_0 is the radiation wave number, and ϕ_0 is the bistatic angle defined as one-half of the angle between radar transmitter and receiver as viewed from the scattering patch. The second-order bistatic cross sections are characterized by three parts: 1) radiation from the scattering patch, which consists of a single scatter from second-order ocean waves along with two scatters from first-order waves, all of which occur on the ocean surface far from the transmitter and receiver; 2) scattering in which one of two scatters occurs at the ocean surface near the radar transmitter; and 3) scattering in which one of the scatters is near the receiver. In parts 2) and 3), the second scatter occurs on the remote patch. Thus, the total second-order HF cross section σ_{Total} of the ocean surface contains four components: one first-order portion and the three second-order components. Based upon the assumption of a pulsed radar system, a model for the ocean clutter

Manuscript received November 16, 2004; accepted October 21, 2005. This work was supported by Natural Sciences and Engineering Research Council under Grant NSERC 238263-01 to Dr. E. Gill, Memorial University of Newfoundland. **Associate Editor: L. R. Wyatt**.

The authors are with Faculty of Engineering and Applied Science, Memorial University of Newfoundland, St. John's, NL A1B 3X5, Canada (e-mail: zhang@engr.mun.ca; egill@engr.mun.ca).

Color versions of one or more of the figures in this paper are available online at http://ieeexplore.ieee.org.

Digital Object Identifier 10.1109/JOE.2006.886201

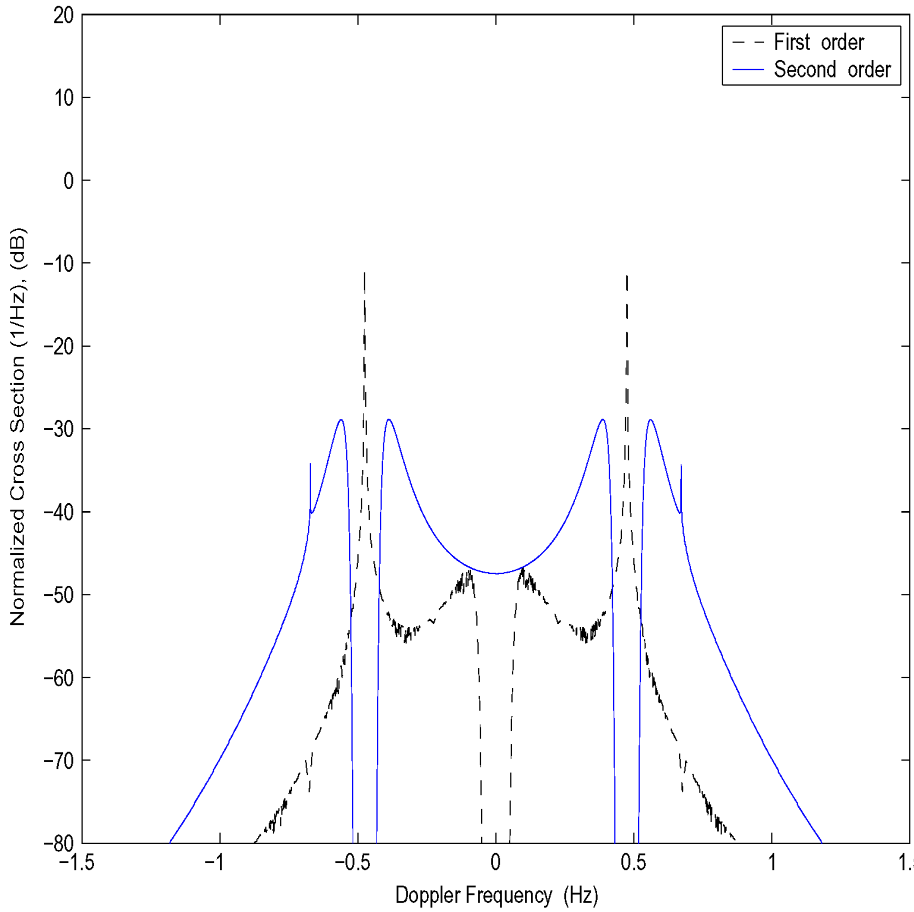

Fig. 1. Simulated bistatic first- and second-order cross sections of the patch scatter with the wind perpendicular to the scattering ellipse normal at the patch (see Fig. 2).

signal-to-noise ratio is presented [18], [19]. In this paper, the models developed in [18] and [19] and detailed in [17] and [20] are incorporated in an algorithm for the inverse problem for the bistatic patch scattering of HF radiation from the ocean surface [21]. However, as seen in [17], the portions of the cross section involving scatters near the transmitter and receiver, being typically about 30 dB below the "patch scatter," do not enter the inversion process. Furthermore, the so-called electromagnetic portion of the "patch scatter" which involves two scatters from first-order waves will also not have a significant effect on the inversion process. The reason for this is that the energy in the Doppler region to which the inversion applies is influenced much more strongly by a single scatter from a second-order Bragg wave than by a dual scatter from first-order waves.

In Section II, bistatic cross sections are depicted. The new inversion algorithm is presented in Section III. The effect of different water depths, wind directions, wind speeds, and radar frequencies are considered. In Section IV, the effect of zero-mean stationary Gaussian noise external to the system is examined with conclusions appearing in Section V.

II. Simulation of the Bistatic Cross Sections

A. *Normalized Cross-Section Equations*

The ocean surface layer is a dispersive medium for wind-driven gravity waves, and the phase speeds of these waves are proportional to their wavelengths. The relationship between the radian frequency ω of an ocean wave, and the corresponding wave number k is (see, for example, [22])

$$\omega = \sqrt{gk\tanh(dk)} \tag{1}$$

where g is the acceleration due to gravity and d is water depth. The position of the first-order peaks in the Doppler spectrum (see Fig. 1) matches the velocities of ocean waves whose wavelengths are equal to one-half the radar operating wavelength if grazing incidence and monostatic operation are assumed. Thus, for water waves traveling toward and away from the radar, the Doppler frequencies of the first-order peaks will occur at

$$\omega_B = \pm\sqrt{2gk_0\tanh(2dk_0)}. \tag{2}$$

Of course, underlying ocean currents will cause a displacement of these peaks from the given theoretical positions. For deep water, in which the water depth is greater than approximately one-half of the ocean wavelength, the hyperbolic tangent approaches unity, and the dispersion relationship in (1) simplifies to

$$\omega = \sqrt{gk} \tag{3}$$

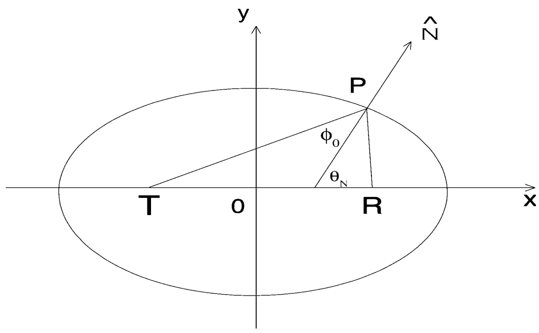

Fig. 2. Geometry of the bistatic configuration. Transmitter (T) and receiver (R) are foci of an elliptical scattering patch. P is a scatter position on this ellipse where the unit normal is $\hat{N}$, while θ_N is the direction of the dominant scattering wave vector and ϕ_0 is defined as the bistatic angle.

while the Doppler frequencies of the first-order peaks become from (2)

$$\omega_B = \pm\sqrt{2gk_0}. \tag{4}$$

The geometry of the bistatic configuration is depicted in Fig. 2. The path directed from the transmitter (T) to the receiver (R) is the baseline reference (x-axis). T and R are foci of an elliptical scattering patch. P is a position on this ellipse where the unit normal is $\hat{N}$. The angle θ_N from $\overline{TR}$ to the unit normal is precisely the direction of the dominant scattering wave vector in the first-order cross section. The angle $\angle TPR$ is bisected by the ellipse normal and one-half of this is defined as the bistatic angle ϕ_0.

For bistatic scattering, the Doppler frequencies of the first-order peaks are a function of ϕ_0 as given by [17]

$$\omega_B = \pm\sqrt{2gk_0\cos\phi_0\tanh(2dk_0\cos\phi_0)}. \tag{5}$$

Of course, for deep water

$$\omega_B = \pm\sqrt{2gk_0\cos\phi_0}. \tag{6}$$

In order that the analysis may be readily used for any operating frequency of interest, the bistatic first-order and second-order cross sections developed by Gill and Walsh [17] are normalized and calculated. The normalizing factor is $2k_0\cos\phi_0$. Then, the normalized wave vector is

$$\vec{K} = \frac{\vec{k}}{2k_0\cos\phi_0} \tag{7}$$

and the normalized wave number is

$$K = \frac{k}{2k_0\cos\phi_0}. \tag{8}$$

For consistency, the other dimensionless quantities of normalization are obtained as follows:

— normalized water depth D

$$D = 2dk_0\cos\phi_0; \tag{9}$$

— normalized Doppler frequency η

$$\eta = \frac{\omega}{\omega_B} = \frac{\sqrt{gk\tanh(kd)}}{\sqrt{2gk_0\cos\phi_0\tanh(2dk_0\cos\phi_0)}} = \frac{\sqrt{K\tanh(KD)}}{\sqrt{\tanh D}}; \tag{10}$$

— normalized ocean wave spectrum $Z_1(\cdot)$

$$Z_1(m\vec{K}) = (2k_0\cos\phi_0)^4 S_1(m\vec{k}). \tag{11}$$

Then, the first-order cross section in normalized form is given as

$$\sigma_1(\eta) = \omega_B\sigma_1(\omega) = 8\pi k_0 \sum_{m=\pm1} Z_1(m\vec{K}) \times K^{\frac{5}{2}}\Delta\rho_s Sa^2[\Delta\rho_s k_0(K-1)] \tag{12}$$

where $\Delta\rho_s$ is the scattering patch width illuminated by a radar pulse, Sa is the sampling function, while $m=\pm1$ indicates the positive and negative Bragg regions corresponding to ocean waves moving along $\pm\hat{N}$, where $\hat{N}$ is the ellipse normal at a particular scattering position (see Fig. 2).

For water of arbitrary depth, the normalized version of the second-order cross section is

$$\sigma_{2p}(\eta) = 4\pi^2 \sum_{m_1=\pm1}\sum_{m_2=\pm1}\int_{-\pi}^{\pi}\int_0^{\infty} Z_1(m_1\vec{K}_1) \times Z_1(m_2\vec{K}_2)|{}_S\Gamma_p|^2\delta(\eta+m_1\eta_1+m_2\eta_2) \times K_1 dK_1 d\theta_{\vec{K}_1} \tag{13}$$

where

$$\eta_1 = \frac{\sqrt{K_1\tanh(K_1D)}}{\sqrt{\tanh(D)}}$$
$$\eta_2 = \frac{\sqrt{K_2\tanh(K_2D)}}{\sqrt{\tanh(D)}}.$$

${}_S\Gamma_p$ is the normalized coupling coefficient, $\delta(\cdot)$ is the usual delta function, and $\theta_{\vec{K}_1}$ is the mean direction of one of the scattering ocean wave. The constraint on the normalized scattering wave numbers so that the second-order scattering will occur is

$$\vec{K}_1 + \vec{K}_2 = \vec{K} \tag{14}$$

where $\vec{K}$ has the direction of the scattering ellipse normal and a magnitude of unity. From the law of cosines, K_2 is expressed in terms of K_1 as

$$K_2^2 = K_1^2 + 1 - 2K_1\cos\left(\theta_{\vec{K}_1} - \theta_N\right). \tag{15}$$

The dual-integral equation in the second-order cross section is reduced to a single-integral equation by means of the solution of delta function constraint. The Newton–Raphson method is invoked to derive the wave number K_1 for each wave frequency η and scattering angle $\theta_{\vec{K}_1}$ [8], [9]. After a trivial calculation, the normalized second-order cross section is simplified as

$$\sigma_{2p}(\eta) = 8\pi^2 \sum_{m_1=\pm1}\sum_{m_2=\pm1}\int_{-\pi}^{\pi} Z_1(m_1\vec{K}_1) \times Z_1(m_2\vec{K}_2)|{}_S\Gamma_p|^2 J_t Y^2|_{Y=Y^*} d\theta_{\vec{K}_1} \tag{16}$$

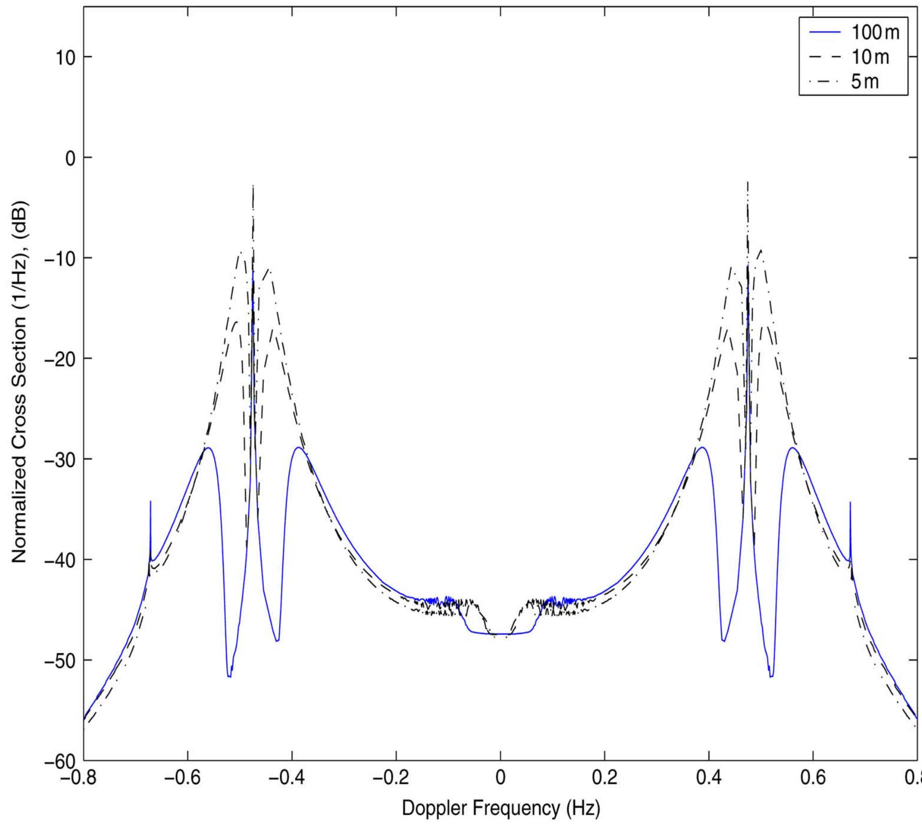

Fig. 3. Bistatic radar cross sections for water depths of 100, 10, and 5 m. 100 m may be viewed as deep water.

where $Y = \sqrt{K_1}$, the value Y^* is solution of the delta function constraint, and J_t is the normalized Jacobian of the transformation which has the form

$$J_t = \frac{\sqrt{\tanh(D)}}{|J_D|} \tag{17}$$

where

$$\begin{aligned} J_D = {} & m_1 \frac{\tanh(Y^2 D) + Y^2 D \mathrm{sech}^2(Y^2 D)}{\sqrt{\tanh(Y^2 D)}} \\ & + m_2 \frac{Y^3 - Y\cos\left(\theta_{\vec{K}_1} - \theta_N\right)}{K_2^{\frac{3}{2}}} \\ & \times \frac{\tanh(K_2 D) + K_2 D \mathrm{sech}^2(K_2 D)}{\sqrt{\tanh(k_2 D)}}. \end{aligned} \tag{18}$$

The choice of an ocean spectral model for simulation has been discussed by Gill [18]. Generally, ocean spectral models may be considered as a product of a nondirectional spectrum $S_1(k)$, and a normalized directional distribution $g(\theta_{\vec{k}})$, i.e.,

$$S_1(\vec{k}) = S_1(k) g(\theta_{\vec{k}}). \tag{19}$$

For reasons described in [18], $S_1(k)$ is defined by means of the Pierson–Moskowitz spectrum [23] as

$$S_1(k) = \frac{1}{2} S_{PM}(k) \tag{20}$$

where

$$S_{PM}(k) = \frac{\alpha_{PM}}{2k^4} \exp\left(\frac{-0.74 g^2}{k^2 u^4}\right). \tag{21}$$

Here, α_{PM} is a constant with a value 0.0081 while u is the wind speed measured at 19.5 m above the ocean surface. Then, the directional ocean wave spectrum may be written as

$$\begin{aligned} S_1(m\vec{k}) = {} & \left[\frac{\alpha_{PM}}{4k^4} \exp\left(\frac{-0.74 g^2}{k^2 u^4}\right)\right] \\ & \times \left[\frac{4}{3\pi} \cos^4\left(\frac{\theta_{\vec{k}} + \frac{(1-m)\pi}{2} - \theta_w}{2}\right)\right] \end{aligned} \tag{22}$$

where θ_w is the wind direction with respect to the reference direction x-axis. Of course, the directional distribution in the second square bracket of (22) is just a typical value chosen for illustrative purpose. The normalized directional ocean wave spectrum $Z_1(m\vec{K})$ may be obtained by (11).

B. Illustration of σ_1 and σ_2

The scattering geometry associated with the illustration of the bistatic Doppler radar spectra presented in Figs. 3–6 may be referenced to Fig. 2 as follows: The ellipse normal is chosen as 90°, wind directions are indicated, and the bistatic angle is 30°. Of course, all the angles are with respect to the x-axis.

Fig. 3 depicts the water-depth dependence of the first- and second-order bistatic cross sections of patch scatter with illustrations given for depths of 100 (deep water), 10, and 5 m. The

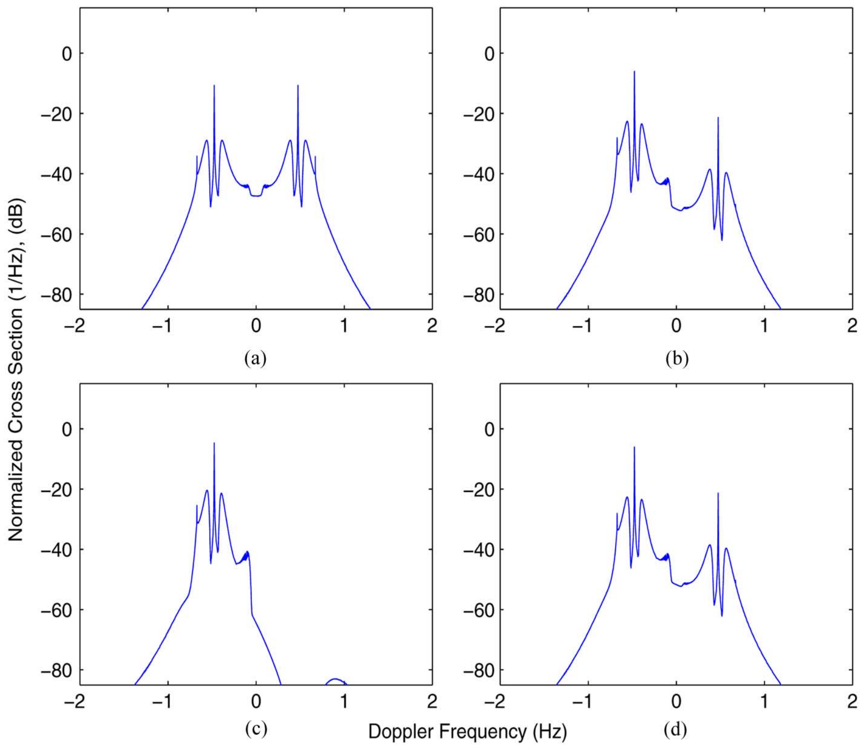

Fig. 4. Bistatic radar cross sections for a wind speed of 15 m/s and wind directions of (a) $\theta_w = 0°$, (b) $\theta_w = 45°$, (c) $\theta_w = 90°$, and (d) $\theta_w = 135°$ to x-axis.

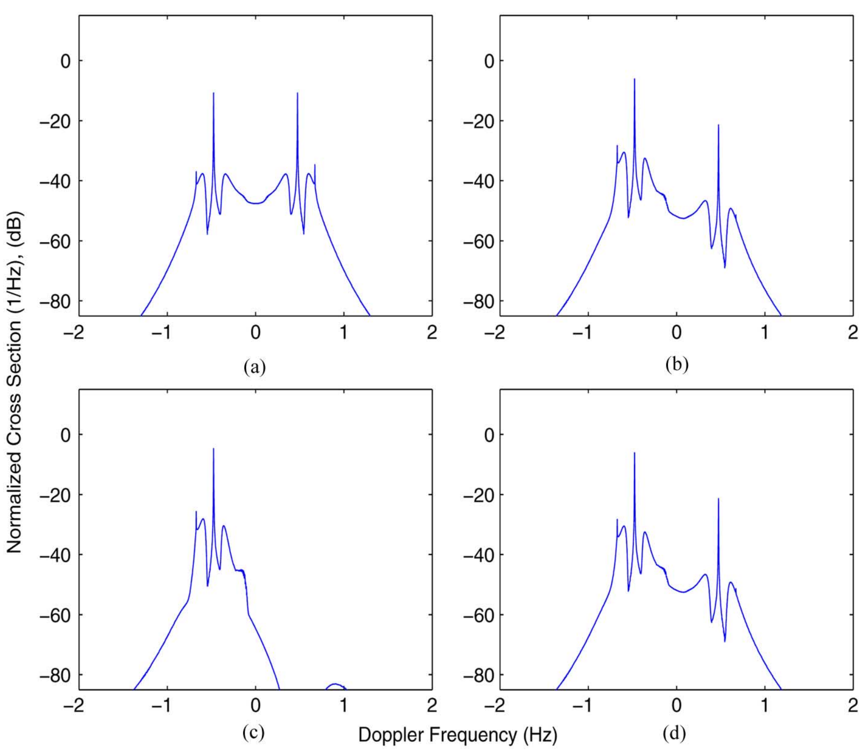

Fig. 5. Bistatic radar cross sections for wind speed of 10 m/s and wind directions of (a) $\theta_w = 0°$, (b) $\theta_w = 45°$, (c) $\theta_w = 90°$, and (d) $\theta_w = 135°$ to x-axis.

radar operating frequency is 25 MHz. The wind speed is 15 m/s at 0° to the x-axis.

Fig. 4 depicts the bistatic cross sections with wind directions θ_w =0°, 45°, 90°, and 135°. 25 MHz is used as the radar operating frequency. The wind directions of 45° and 135° are symmetrical with respect to the ellipse normal and produce identical results. This is analogous to the well-known directional ambiguity associated with winds which are symmetric about the radar look direction in monostatic operation.

Fig. 5 gives the bistatic cross sections for wind speeds of $u = 10$ m/s. The radar operating frequency is 25 MHz. As expected, a significant reduction in the second-order cross sec-

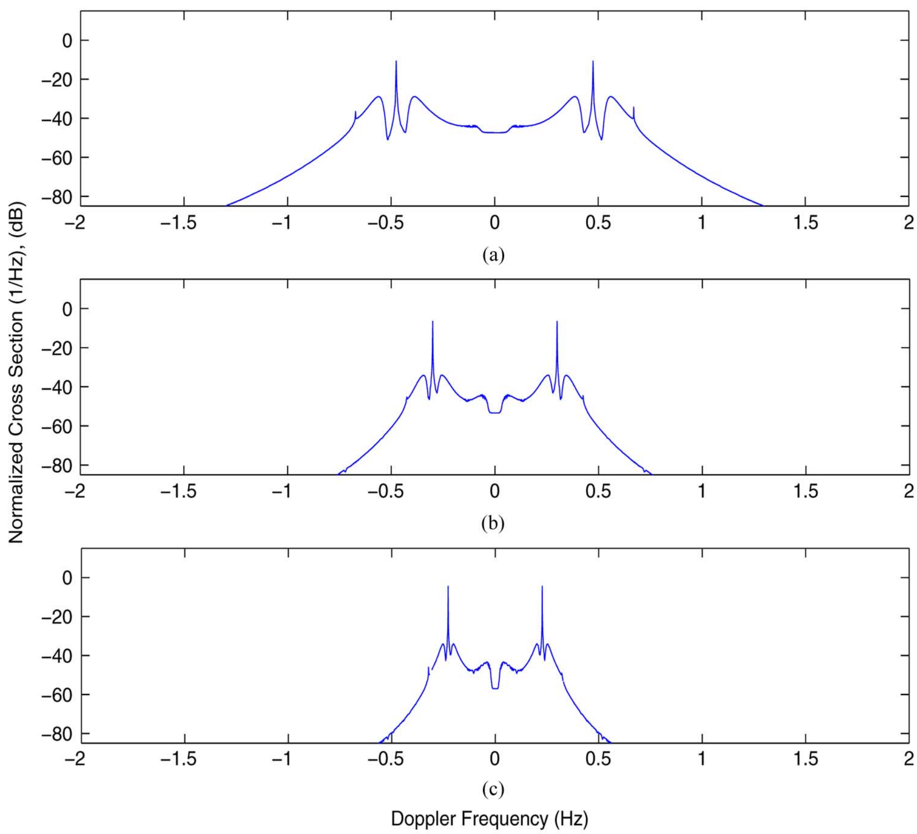

Fig. 6. Bistatic radar cross sections for (a) 25 MHz, (b) 10 MHz, and (c) 5.75 MHz radar operating frequency. The wind speed is 15 m/s, 0° to the x-axis.

tion (as compared to that for $u = 15$ m/s) occurs as sea state decreases.

Fig. 6 depicts the bistatic first- and second-order cross sections for different radar operating frequencies. The wind speed is 15 m/s and the same wind direction, water depth, and bistatic angle are used. In the second-order region, when the radar frequency is 25 MHz, the continuum adjacent to the Bragg peaks is quite distinct. This means that much of the ocean spectral energy is mapped to these regions. When the radar frequency is 5.75 MHz, the second-order curve is not as distinct in the near-Bragg regions because there is significantly less spectral energy being mapped to the corresponding regions. The different behaviors of the second-order cross section in the near Bragg regions for higher and lower radar operating frequencies will significantly affect the inversion results as will be seen in Section III.

III. Inverse Analysis

In this section, the integral equation of the bistatic second-order cross section is inverted to obtain the nondirectional ocean wave spectrum. The influence from ocean currents is neglected, but could be trivially included. The nonlinear factor inside the integrand is linearized under the assumption that the selected Doppler frequency ranges are close to the first-order peaks. The corresponding ocean wave frequency ranges will contain the predominant portion of the ocean wave spectrum when the radar is operated in the upper half of the HF band.

The inversion of the integral equation is carried out numerically in a manner similar to that in [9]. A frequency band approximation is invoked to discretize the integral equation and to convert it to a matrix equation. The directional ocean wave spectrum is represented by a truncated Fourier series. Nondirectional ocean wave spectra for different ocean conditions are derived and discussed.

A. Selection of the Ocean Wave Number Range

The nonlinearity of the integrand of the second-order cross section [see (16)] comes from the product of two unknown but related factors $Z_1(m_1\vec{K}_1)$ and $Z_1(m_2\vec{K}_2)$. Lipa and Barrick [11] used the assumption that for $K_1 \ll K_2$, the wave of $\vec{K}_2$ is in the saturated region of the ocean wave spectrum along with the Bragg wave. In this region, the magnitude of $\vec{K}_2$ will be approximately equal to the magnitude of Bragg wave $\vec{K}_B$. To specify the region, it is useful to define a dimensionless parameter μ, which is the magnitude of the normalized Doppler frequency shifted from the first-order peaks, i.e.,

$$\mu = -m_1(\eta + m_2). \tag{23}$$

Within the range $\mu < 0.4$, the linear assumption is satisfied [11].

The range of μ is used to determine the range of frequency that will be selected for the inverse analysis. From (23) and since $m_1 = (1/m_1)$ for $m_1 = \pm 1$, we have

$$\eta = -m_1\mu - m_2. \tag{24}$$

If the range of μ is known, so is the range of η for various combinations of m_1 and m_2. In the algorithm that is described in this paper, the range of μ is selected as $0.05 < \mu < 0.36$.

Lipa and Barrick [11] provide a method to derive the boundaries of the corresponding wave number bands. They show that, for deep water, the lower and upper limitations of the wave number band K_{1L} and K_{1U}, associated with the values of μ are

$$K_{1L} \approx \mu^2 - \mu^3 \tag{25}$$

and

$$K_{1U} \approx \mu^2 + \mu^3. \tag{26}$$

B. Linearization Method

The integrand of (16) is nonlinear in wave number by virtue of the ocean spectral product. Here, a linearization scheme pioneered by Lipa and Barrick [9], [24] and successfully used by many other investigators (see, for example, [16]) is followed. The method requires that the wave vector $\vec{K}_2$ lies in the saturated region of ocean wave spectrum. In this scheme, the nondirectional wave spectra $Z_1(m_1\vec{K}_1)$ and $Z_1(m_2\vec{K}_2)$ are represented by the Fourier coefficients, i.e.,

$$Z_1(m_1\vec{K}_1) = \frac{1}{2\pi}\sum_{n_1=0}^{\infty}\Big[a_{n_1}(m_1,K_1)\cos\left(n_1\theta_{\vec{K}_1}\right) + b_{n_1}(m_1,K_1)\sin\left(n_1\theta_{\vec{K}_1}\right)\Big] \tag{27}$$

and

$$Z_1(m_2\vec{K}_2) = \frac{1}{2\pi}\sum_{n_2=0}^{\infty}\Big[a_{n_2}(m_2,K_2)\cos\left(n_2\theta_{\vec{K}_2}\right) + b_{n_2}(m_2,K_2)\sin\left(n_2\theta_{\vec{K}_2}\right)\Big]. \tag{28}$$

Since the directional wave spectra are even functions of wind direction only the cosine terms of Fourier coefficients are needed in the expansions. Then, (27) and (28) are simplified as

$$Z_1(m_1\vec{K}_1) = \frac{1}{2\pi}\sum_{n_1=0}^{\infty}\Big[a_{n_1}(m_1,K_1)\cos\left(n_1\theta_{\vec{K}_1}\right)\Big] \tag{29}$$

and

$$Z_1(m_2\vec{K}_2) = \frac{1}{2\pi}\sum_{n_2=0}^{\infty}\Big[a_{n_2}(m_2,K_2)\cos\left(n_2\theta_{\vec{K}_2}\right)\Big] \tag{30}$$

respectively. Using the linearization scheme which invokes a Phillips equilibrium spectrum, $a_{n_2}(m_2,K_2)$ in (30) is converted to the corresponding Fourier coefficients as

$$a_{n_2}(m_2,K_2) = \frac{a_{n_2}(m_2,K_B)}{K_2^4} \tag{31}$$

where $K_B = 1$.

Considering that the upper limits of the Fourier series summation in (29) and (30) should be finite for numerical calculation, a truncation value of two is used following the suggestion of previous investigators (see, for example, [16]). The linearized second-order bistatic cross section may be written from (16) and (29)–(31) as

$$\begin{aligned}\sigma_{2pL}(\eta) = 2\sum_{m_1=\pm1}\sum_{m_2=\pm1}\int_{-\pi}^{\pi}\sum_{n_1=0}^{2}\sum_{n_2=0}^{2}\Big[a_{n_1}(m_1,K_1) \\ \times\cos\left(n_1\theta_{\vec{K}_1}\right)\Big] \\ \times\Big[a_{n_2}(m_2,1)\cos\left(n_2\theta_{\vec{K}_2}\right)\Big]\left|{}_S\Gamma_p\right|^2 J_t\frac{K_1^{\frac{3}{2}}}{K_2^4}d\theta_{\vec{K}_1}\end{aligned} \tag{32}$$

with the Fourier coefficients being

$$a_{n_1}(m_1,K_1) = \int_0^{2\pi} Z(m_1\vec{K}_1)\cos\left(n_1\theta_{\vec{K}_1}\right)d\theta_{\vec{K}_1}. \tag{33}$$

For $n_1 = 2$, we have

$$a_0(m_1,K_1) = \int_0^{2\pi} Z(m_1\vec{K}_1)d\theta_{\vec{K}_1} \tag{34}$$

$$a_1(m_1,K_1) = \int_0^{2\pi} Z(m_1\vec{K}_1)\cos\left(\theta_{\vec{K}_1}\right)d\theta_{\vec{K}_1} \tag{35}$$

and

$$a_2(m_1,K_1) = \int_0^{2\pi} Z(m_1\vec{K}_1)\cos\left(2\theta_{\vec{K}_1}\right)d\theta_{\vec{K}_1}. \tag{36}$$

A question which may be legitimately proposed now is "Why approach the problem of inversion using Fourier series methods?" The answer lies partially in the fact that, as detailed by Barrick and Lipa [25], some of the important spectral parameters are linked directly to the Fourier coefficients of the ocean surface which result from the inversion. For example, the Fourier coefficient $a_0(m_1,K_1)$ is of particular importance since it essentially gives the nondirectional ocean wave spectrum. Other parameters linked to higher order coefficients involve the mean wave direction and the spreading parameter.

C. Discretization of the Integral Equation

As can be seen from the expression for the cross section in (32), for each value of η, K_1 changes with the angle $\theta_{\vec{K}_1}$. To discretize the integral, the continuous wave number values are separated into bands of equal size. The wave numbers are assumed constant within a given band, with the central value being used as the representative wave number. This is the wave number band approximation suggested by Lipa and Barrick [11]. For each wave number band, the ocean wave spectrum can be represented by its corresponding Fourier series component. The integral is obtained by calculating the summation of values inside each wave number band. The procedure is outlined as follows.

For J wave number bands, the boundaries are obtained from (25) and (26). The wave numbers for each band are equally spaced. For a specific Doppler frequency value, $\eta = \eta_s, \theta_{\vec{K}_1}$

changes from θ_L to θ_U. The related set of scattering wave numbers is calculated. Each wave number belongs to a certain wave number band, and there are Q wave number bands associated with each η_s (where $Q \leq J$). For the a_0 coefficient of the Fourier series, we have

$$\begin{aligned}\sigma_{2pL}(\eta_s)|_{a_0} &= \sum_{m_1=\pm 1} [a_0(m_1, K_{1,1})F_{a_0 1} + a_0(m_1, K_{1,2})F_{a_0 2} + \cdots \\ &+ a_0(m_1, K_{1,q})F_{a_0 q} + \cdots + a_0(m_1, K_{1,Q})F_{a_0 Q}]\end{aligned} \tag{37}$$

where $F_{a_0 q}$ is defined as

$$\begin{aligned}F_{a_0 q} = 2 \sum_{m_2=\pm 1} \sum_{n_2=0}^{2} \int_{\theta_{q-1}}^{\theta_q} & \Big[a_{n_2}(m_2, 1) \\ & \times \cos\left(n_2 \theta_{\vec{K}_2}\right)\Big] |_S\Gamma_p|^2 J_t \frac{K_1^{\frac{3}{2}}}{K_2^4} d\theta_{\vec{K}_1}.\end{aligned} \tag{38}$$

The second-order cross section contains four parts as indicated by the various combination of m_1 and m_2. It is convenient to denote the groups of the selected normalized Doppler frequencies by μ. Each μ determines four Doppler frequencies from the four portions of the cross section, respectively. Letting the total number of μ be I means that $4I$ values of frequency η are being used. Consequently, the integral equation of the linearized second-order cross section may be represented by a matrix equation

$$CX = B \tag{39}$$

where X is a column array with its elements being the Fourier coefficients corresponding to each wave frequency band, i.e.,

$$X = [{}_1x {}_2x \cdots {}_jx \cdots {}_Jx]^T \tag{40}$$

with the element ${}_jx$ being

$${}_jx = [{}_ja_0(m_1, K_1)\, {}_ja_1(m_1, K_1)\, {}_ja_2(m_1, K_1)]^T. \tag{41}$$

B is a column array with its elements being the simulated radar data selected for inversion. It may be represented as

$$B = [B(\mu_1)B(\mu_2)\cdots B(\mu_i)\cdots B(\mu_I)]^T \tag{42}$$

where the element $B(\mu_i)$ contains the ith set of four cross section components as indicated by

$${}_iB(\mu_i) = [{}_i\sigma(\eta_{P_1})_i\, \sigma(\eta_{P_2})_i\, \sigma(\eta_{P_3})_i\, \sigma(\eta_{P_4})]^T. \tag{43}$$

where the indices P_1, P_2, P_3, and P_4 denote the four parts of the second-order cross section.

Matrix C, the kernel matrix, has $4I$ row corresponding to the number of selected frequencies. The number of columns is equal to the number of frequency bands J times the number of the Fourier coefficients. Thus, the kernel matrix has a dimension of $4I \times 3J$.

The arrangement of elements in the kernel matrix C is critical to the stability of the subsequent inversion. Analogous to similar decision by Gill and Walsh [16] for a widebeam radar application, matrix C may be arranged as

$${}_{i,j}C = \begin{bmatrix} \int_{P_1} F_{a_0 ij} d\theta_{\vec{K}_1} & \int_{P_1} F_{a_1 ij} d\theta_{\vec{K}_1} & \int_{P_1} F_{a_2 ij} d\theta_{\vec{K}_1} \\ \int_{P_2} F_{a_0 ij} d\theta_{\vec{K}_1} & \int_{P_2} F_{a_1 ij} d\theta_{\vec{K}_1} & \int_{P_2} F_{a_2 ij} d\theta_{\vec{K}_1} \\ \int_{P_3} F_{a_0 ij} d\theta_{\vec{K}_1} & \int_{P_3} F_{a_1 ij} d\theta_{\vec{K}_1} & \int_{P_3} F_{a_2 ij} d\theta_{\vec{K}_1} \\ \int_{P_4} F_{a_0 ij} d\theta_{\vec{K}_1} & \int_{P_4} F_{a_1 ij} d\theta_{\vec{K}_1} & \int_{P_4} F_{a_2 ij} d\theta_{\vec{K}_1} \end{bmatrix} \tag{44}$$

where $F_{a_1 ij}$ and $F_{a_2 ij}$ are of the form of the expressions in (38). This is an effective but not unique way to arrange the elements of C. A numerical simulation has validated this construction of C as a successful choice. The number of frequency bands is chosen as 60 and the Fourier series representation is truncated at $n = 2$. The number of selected frequency groups is taken to be approximately $\mu = 120$, and for that choice, matrix C has dimensions of 480×180.

D. SVD Solution of the Matrix Equation

Ideally, the problem of solving a matrix equation such as (39) means determining

$$X = C^{-1}B \tag{45}$$

where C^{-1} is the inverse of C. If the inverse matrix C^{-1} does not exist or if it has a large condition number as a result of it being the discretization of an ill-posed system, there will be no unique solution for X. However, this kind of matrix equation may still be solved approximately. Instead of finding the inverse matrix C^{-1}, the SVD method (e.g., see [26]) is invoked to find a pseudoinverse matrix C^+ for the kernel matrix C. Then

$$X = C^+B. \tag{46}$$

This result denotes a *linear least-squares solution*.

In setting up the SVD routine, it is noted that for any real $(n \times m)$ matrix C, there exists orthogonal matrices U and V, with dimensions $m \times m$ and $n \times n$, respectively, which satisfy

$$U^TCV = \begin{bmatrix} \Sigma & \dots & 0 \\ \vdots & \ddots & \vdots \\ 0 & \dots & 0 \end{bmatrix} \tag{47}$$

where U^T is the transpose of U and Σ is a diagonal matrix with nonzero, positive elements $\mu_1, \mu_2, \dots, \mu_n$ satisfying

$$\mu_1 \geq \mu_2 \geq \dots \geq \mu_n \geq 0. \tag{48}$$

The elements $\mu_1, \mu_2, \dots, \mu_n$ are referred to as the singular values of C and are square roots of the eigenvalues of C^TC, where the superscript again indicates "transpose," when C is

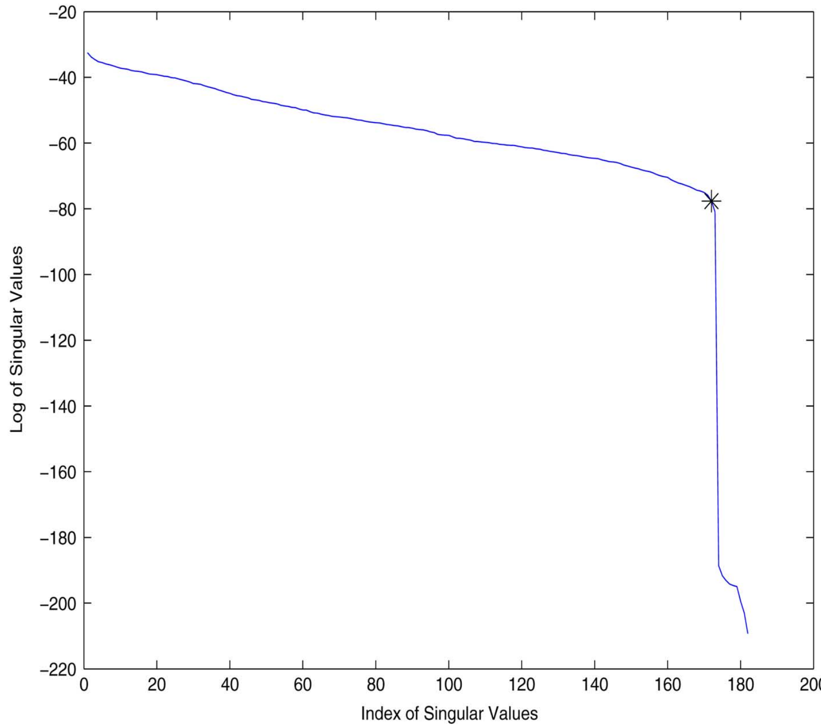

Fig. 7. Example of the choice of the retained number of singular values. The asterisk indicates the position of the retained number ($r = 172$ here).

real. The columns of U and V are the so-called right and left singular vectors of C. From (47), C^+ is

$$C^+ = V \begin{bmatrix} \Sigma^{-1} & \dots & 0 \\ \vdots & \ddots & \vdots \\ 0 & \dots & 0 \end{bmatrix} U^T. \tag{49}$$

A Matlab [27] function *svd* is invoked to calculate the singular values of C to obtain C^+. The Fourier coefficient $a_0(K_1)$ is obtained from the solution of X as the ocean wave nondirectional spectrum.

The determination of how many of the singular values of the kernel matrix C should be retained is another important issue. Beyond a certain number, the singular values will be truncated because they decrease significantly in magnitude and introduce instability in the inversion process. This problem has been well investigated by Howell and Walsh [15]. Generally speaking, the retained number, denoted as r, is chosen as a number equal to or less than the rank of the matrix. In the results presented in Section III-E, the value of r is selected to be equal to the rank of matrix C. The rank of the ill-conditioned matrix is calculated by a Matlab [27] function *rank*. Fig. 7 depicts a typical behavior of the singular values. The retained number $r = 172$ is denoted by an "$*$."

At this stage, it is worthwhile to point out that the choice of such a large number of Doppler frequency bands, in this case 480, and the ocean wave number resolution within each band, is not necessarily optimal, and is used here only for illustrative purposes. In reality, imposing such a fine resolution may exacerbate the problem of an already ill-conditioned system, the latter being largely due to many small values sporadically scattered throughout the kernel matrix [28]. This problem may be mitigated somewhat by grouping the rows of the kernel according to the absolute value of the difference between a particular Doppler frequency and the corresponding Bragg frequency, as in (44). For the case of field data, to which it is intended that the algorithm will be eventually applied, a much smaller kernel matrix will likely yield more stable inversions. In fact, good results have been regularly attained using this method for significant waveheight and nondirectional spectra recovery from both narrowbeam and broadbeam monostatic field data (see, for example, [15] and [16]). Although it is not the subject of this work, it is worthy of note that a more robust algorithm for recovering directional spread information has been successfully implemented by Atanga and Wyatt [29]. In reaching their conclusion, the authors of that work provide an extensive comparison of their method with that used here and in [15]. The application of the newer techniques presented in [29] to the bistatic case, while not addressed here, is intended for future investigation.

E. *Illustration of the Results*

In illustrating the nondirectional ocean wave spectra obtained from the inverse analysis, the bistatic angle is fixed at 30°. The scattering ellipse normal is 90° (see Fig. 2). Several sets of plots, corresponding to different water depths, wind directions, wind speeds, and radar frequencies are obtained and shown. The solid line indicates the recovered wave spectrum, while the dashed line is Pierson–Moskowitz spectrum used in the related cross-section calculation.

Fig. 8 illustrates inversion results for different water depths. The radar frequency is 25 MHz, the wind speed is 15 m/s, and the wind direction is 0° to the x-axis. At this operating frequency, the shallow-water effects begin to affect spectral recovery when the depth is less than 10 m. The effects on

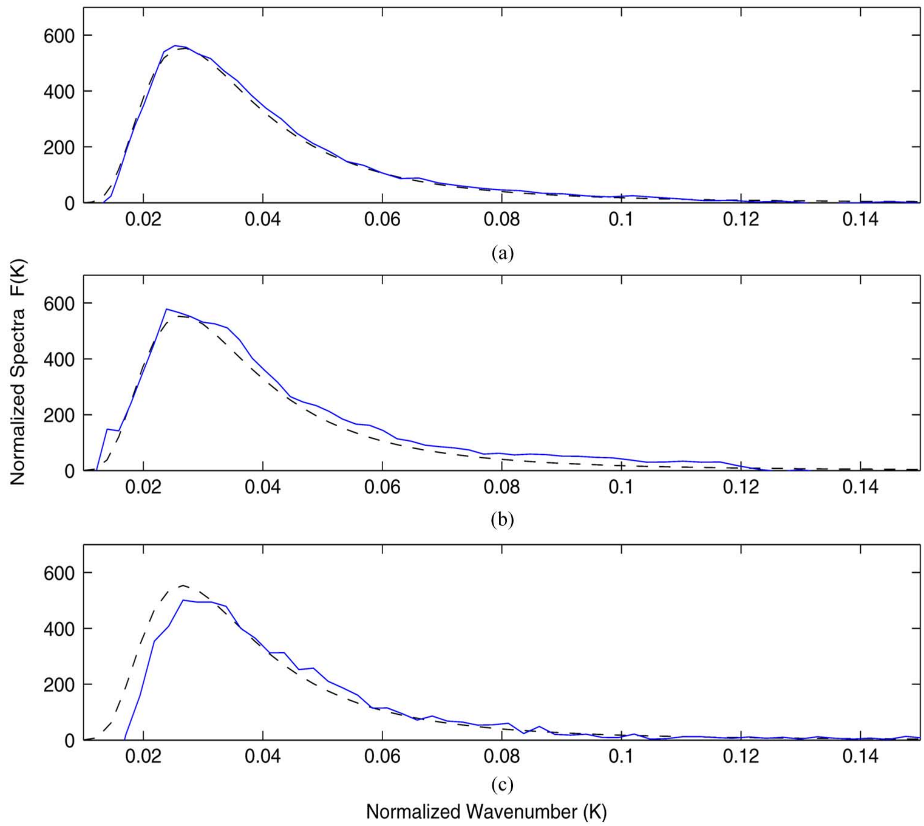

Fig. 8. Recovered nondirectional wave spectra for water depths of (a) 100 m (deep water), (b) 10 m, and (c) 5 m.

magnitude and shape are even more prominent as water depth is further lowered because of the influence from the seafloor. This is not surprising as the underlying assumptions of small height and slope of the surface feature used in developing the cross sections become increasingly less valid as the water becomes shallower.

Fig. 9 depicts the recovered nondirectional spectra for wind directions of 0°, 45°, 90°, and 135° to the x-axis and the wind speed of 15 m/s. The radar frequency is $f_0 = 25$ MHz and the water is deep. When the wind directions are not equal to 90°, the inversion results are well matched with the ideal Pierson–Moskowitz nondirectional spectrum in shape and magnitude. When the wind direction is 90°, which means the wind direction is parallel to the scattering ellipse normal, this match is significantly reduced. The inversion routine sets a threshold of 30 dB between the maximum and minimum useable second-order Doppler data. In the 90° wind direction case (see Fig. 4), this meant two of the four sidebands of the Doppler spectrum could be used in the inversion process. As seen in Section IV, this problem is exacerbated when the data are noisy.

Fig. 10 depicts the recovered ocean wave spectra for wind directions θ_w are 0°, 45°, 90°, and 135° to the x-axis while the wind speed is 10 m/s. The other parameters are the same as for Fig. 9. Here, the recovered shapes do not agree with the ideal nondirectional spectrum as much as when the wind speed is 15 m/s since, for lower sea state, the assumption for linearization is compromised.

Fig. 11 shows comparative results for radar frequencies of 25, 10, and 5.75 MHz. It is observed that almost all the nondirectional ocean wave spectrum is recovered from the Doppler spectrum for a radar frequency of 25 MHz, i.e., the upper level of the HF band. However, as the operating frequency is increased, the higher frequency end of the nondirectional spectrum is not available. This phenomenon may be explained from (25) and (26). These two equations give the normalized lower (K_{1L}) and upper (K_{1U}) wave number boundaries of the recovered spectrum. Since μ is selected in the range $0.05 < \mu < 0.36$, K_{1L} will be

$$K_{1L} = 0.05^2 - 0.05^3 = 0.0024 \tag{50}$$

and K_{1U} will be

$$K_{1U} = 0.36^2 + 0.36^3 = 0.176. \tag{51}$$

When the normalized wave numbers K_{1L} and K_{1U} are converted to the unnormalized versions, they will be multiplied by the factor $2k_0\cos(\phi_0)$, which is a function of the radar operating frequency and the bistatic angle. For a bistatic angle of 30° and a radar frequency of 25 MHz, the range of recovered wave numbers may be $0.0022 < k_1 < 0.160$. For 10 MHz, this range is $0.0008 < k_1 < 0.064$, while for 5.75 MHz the range is $0.0005 < k_1 < 0.037$, i.e., the recovered wave number ranges are reduced when radar frequencies are decreased. Of course, for high sea states, lower frequency operation, which allows for improved range capabilities, would also mitigate the problem of

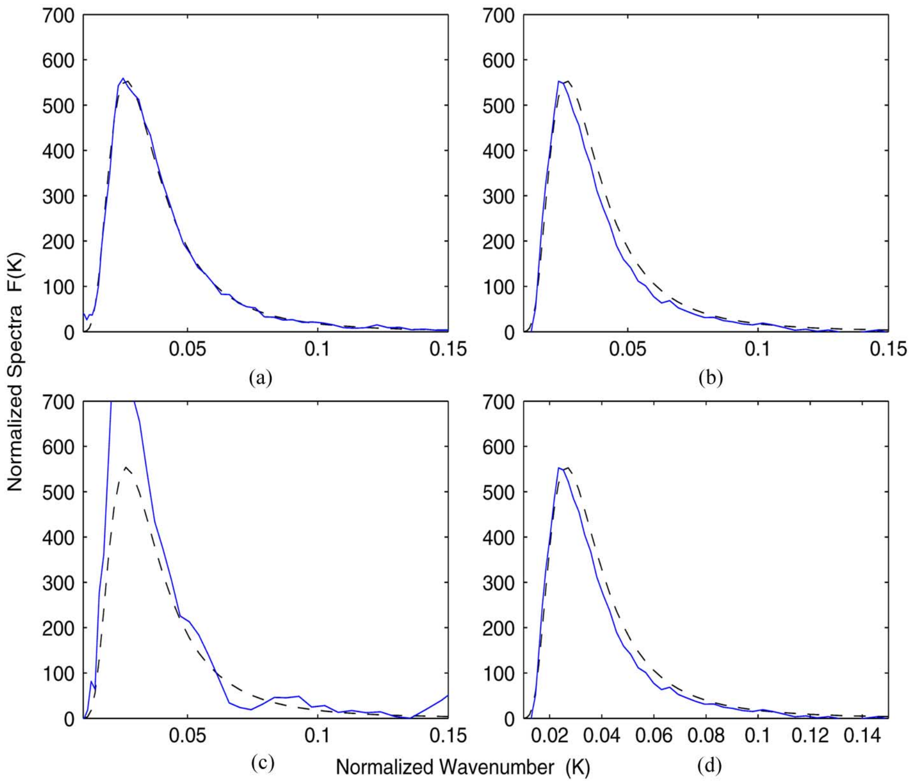

Fig. 9. Recovered nondirectional wave spectra when wind directions are (a) 0°, (b) 45°, (c) 90°, and (d) 135° to the x-axis. Wind speed is kept as 15 m/s. The radar frequency is $f_0 = 25$ MHz.

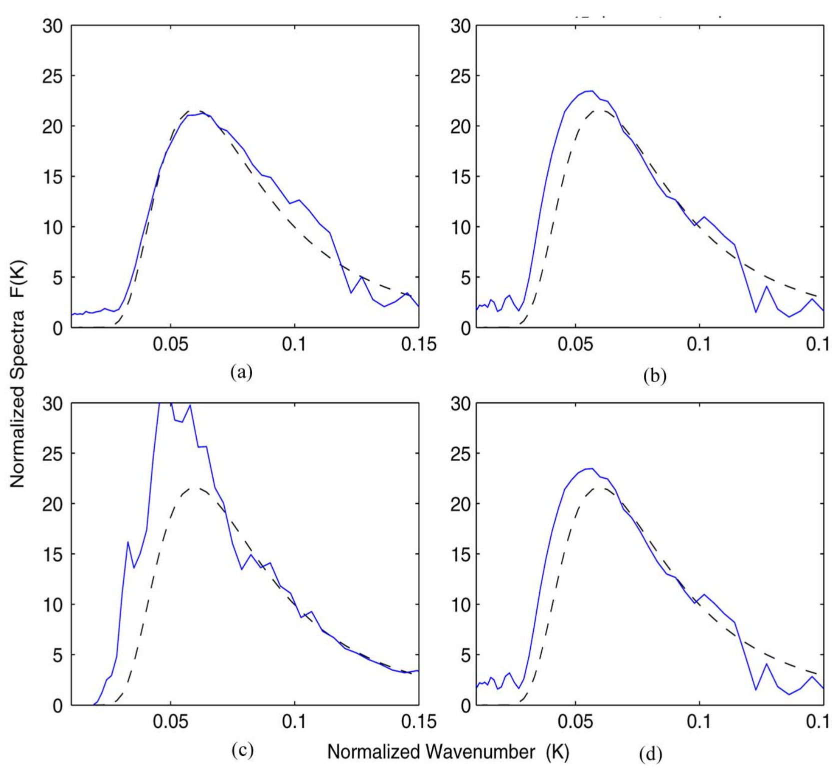

Fig. 10. Recovered nondirectional wave spectra for different wind directions when wind speed is 10 m/s, the radar frequency is $f_0 = 25$ MHz, and wind directions are (a) 0°, (b) 45°, (c) 90°, and (d) 135° to the x-axis.

saturation of the Doppler spectrum and would enhance the recoverability of the ocean spectrum from the radar signal. Thus, for the proposed method, the optimal operating frequency is largely dictated by the waveheights being interrogated and the

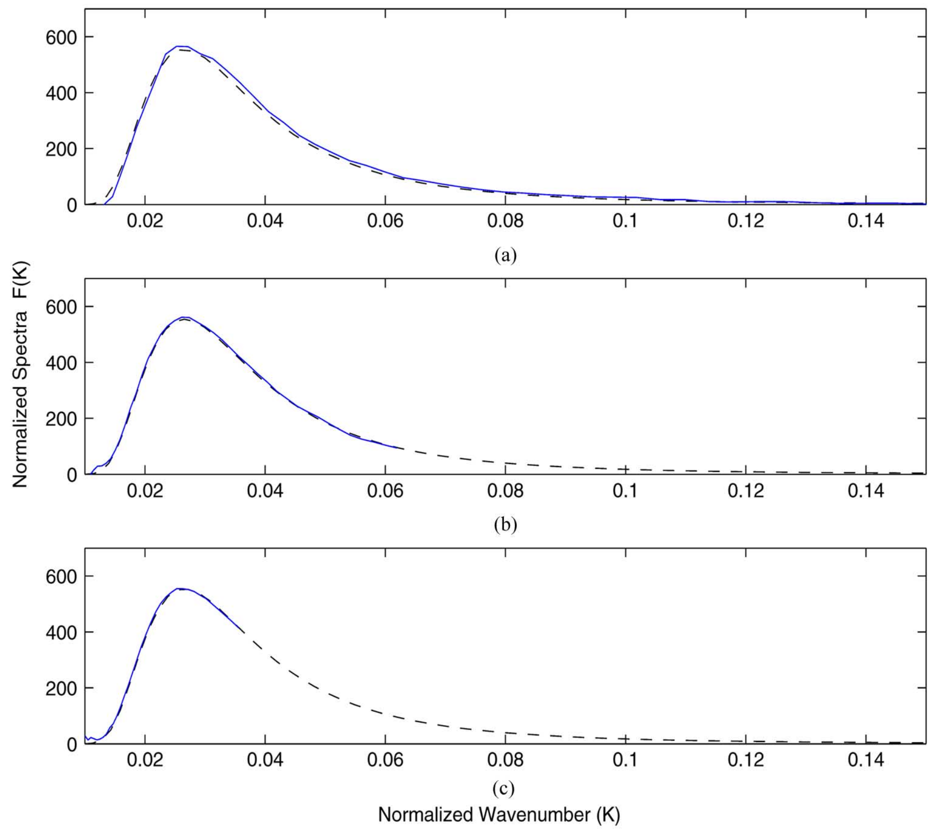

Fig. 11. Recovered nondirectional wave spectra for radar operating frequencies of (a) 25 MHz, (b) 10 MHz, and (c) 5.75 MHz. The wind speed is 15 m/s, 0° to the x-axis.

desired range. These issues may be mitigated somewhat by resorting to a nonlinear inversion scheme that employs a greater extent of the Doppler spectrum in the inversion process. However, for consistency in results, a suitable method for choosing initial parameters to start the inversion process is required [30]. For bistatic operation, the added feature of the bistatic angle dependency dictates further constraints on the combination of ϕ_0 and f_0 such that a significant portion of the ocean spectrum can be recovered.

IV. Model for Noisy Doppler Spectra

A. Simulation of Noisy Bistatic HF Radar Spectra

A model for the simulation of the effect of additive Gaussian white noise for pulsed bistatic radar data is found in [19]. The power spectral density (PSD) of ocean clutter is given as

$$P_c(\eta) = \frac{\lambda_0^2 \left(\dfrac{\tau_0}{T_L}\right) P_t G_t G_r \left|F(\rho_{01}, \omega_0) F(\rho_{02}, \omega_0)\right|^2 A_r \sigma(\eta)}{(4\pi)^3 \rho_{01}^2 \rho_{02}^2}. \tag{52}$$

Here, λ_0 is radar operating wavelength, τ_0 is the pulse width of the transmitted signal, T_L is the pulse repetition period, P_t is the peak power, and G_t and G_r are the gains of transmitting and receiving antennas, respectively. $F(\cdot)$ is the rough spherical earth attenuation function and ρ_{01} and ρ_{02} are the distances from the transmitter and receiver, respectively, to scattering patch. A_r is the patch area, and the normalized patch cross section is $\sigma(\eta) = \sigma_{11}(\eta) + \sigma_{2P}(\eta)$, where $\sigma_{11}(\eta)$ and $\sigma_{2P}(\eta)$ are calculated from (12) and (13).

In keeping with the analysis in [19], for the purpose of illustrating the clutter PSD, the following values are used: $f_0 =$ 25 MHz ($\lambda_0 = 12$ m), $\tau_0 = 13.3$ μs, $T_L = 333$ μs, $P_t = 16$ kW, $G_t = 2$ dB, i ≈ 1.585, $G_r = 56.76$, $\rho_{01} = \rho_{02} = 50$ km, $A_r =$ 702 900 m^2. A 512-point fast Fourier transform (FFT) with 50% overlap and 15 averages are used to calculate the PSD spectrum. Figs. 12–15 depict typical noisy radar Doppler PSD for different water depths, wind directions, wind speeds, and radar operating frequencies. Comparing with Figs. 3–6 in Section II, the ripples over the curve are observed because of the contamination by noise. When the wind speed is 10 m/s or lower and the wind direction is at an angle more than 45°, the second-order part of the positive Doppler PSD is hidden by noise.

B. Recovery of Ocean Wave Spectra

The inverse analysis for noisy data uses the same procedure as explained in Section III. The simulated radar data are produced according to the description in Section IV-A. Figs. 16–19 depict recovered ocean wave spectra for different water depths, wind directions, wind speeds, and radar operating frequencies, associated with Figs. 12–15. Again, the solid line is the recovered wave spectrum, while the dashed line is the original Pierson–Moskowitz spectrum.

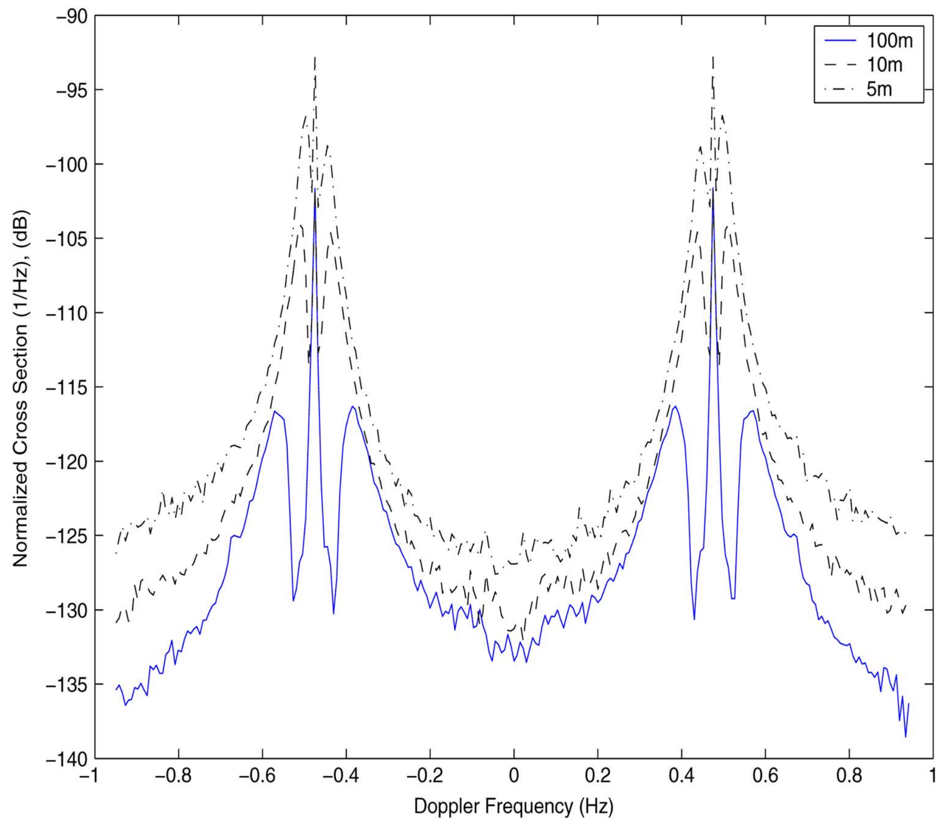

Fig. 12. Simulated noisy spectra for water depths of 100 (deep water), 10, and 5 m (wind speed: 15 m/s; radar frequency: 25 MHz).

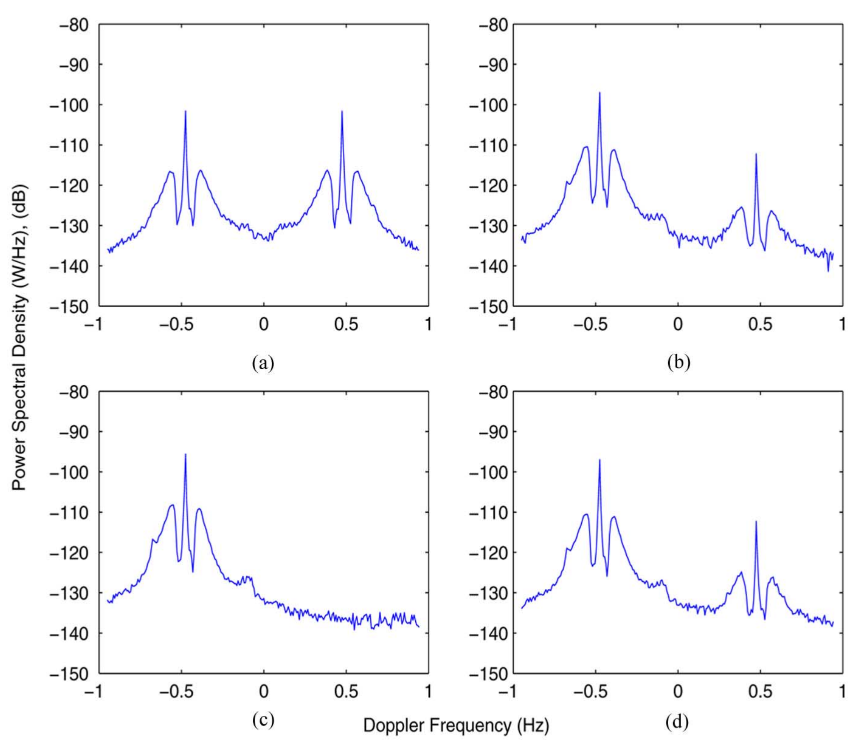

Fig. 13. Simulated noisy spectra for wind directions of (a) $\theta_w = 0°$, (b) $\theta_w = 45°$, (c) $\theta_w = 90°$, and (d) $\theta_w = 135°$ (wind speed: 15 m/s; radar frequency: 25 MHz).

The earlier comments about the inversion results for noise-free sea echo also apply here. The normalized root-mean-square (rms) waveheights for noise- free and noisy spectra at different wind directions are listed in Table I. The same values obtained

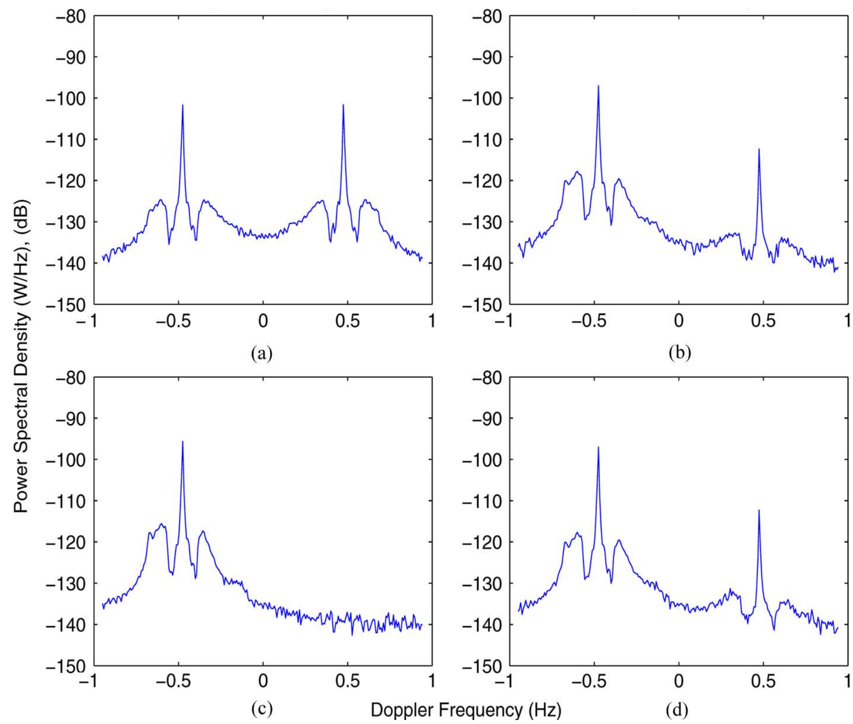

Fig. 14. Simulated noisy spectra for different wind directions when wind speed is 10 m/s, radar frequency is 25 MHz, and wind directions are (a) $\theta_w = 0°$, (b) $\theta_w = 45°$, (c) $\theta_w = 90°$, and (d) $\theta_w = 135°$.

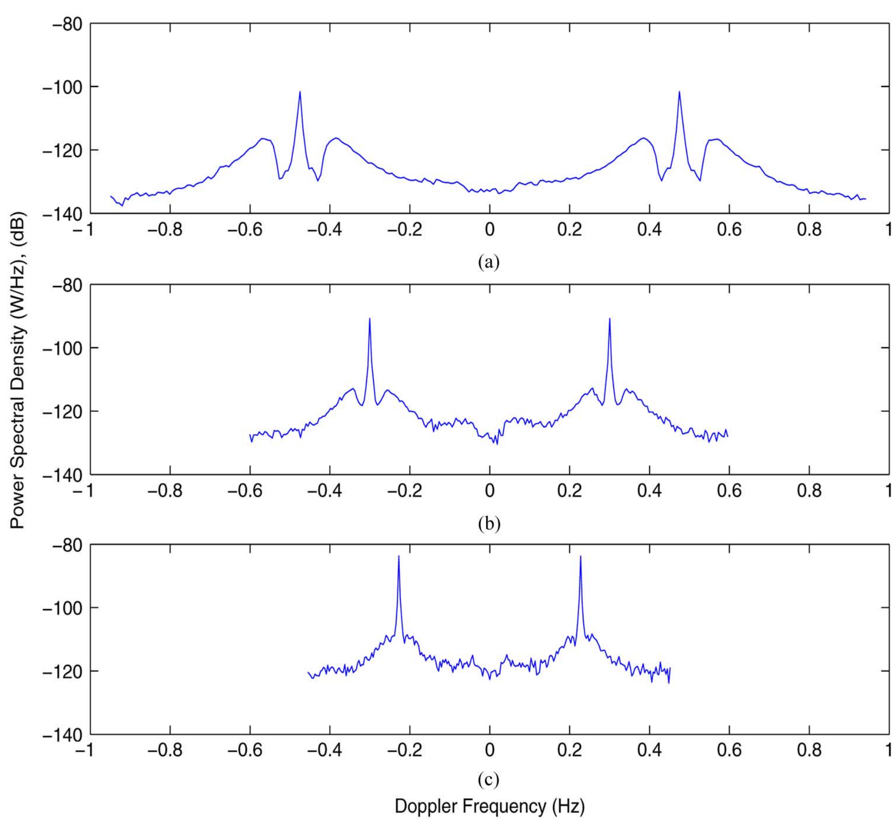

Fig. 15. Simulated noisy spectra for (a) 25 MHz, (b) 10 MHz, and (c) 5.75 MHz radar operating frequency. The wind speed is 15 m/s, 0° to the x-axis.

directly from corresponding Pierson–Moskowitz spectra are also listed as the ground truth when the percent of difference is calculated.

It is obvious that the results from noisy spectra for nondirectional wave spectra and normalized rms waveheights are less well matched to the actual conditions than those from the noise-

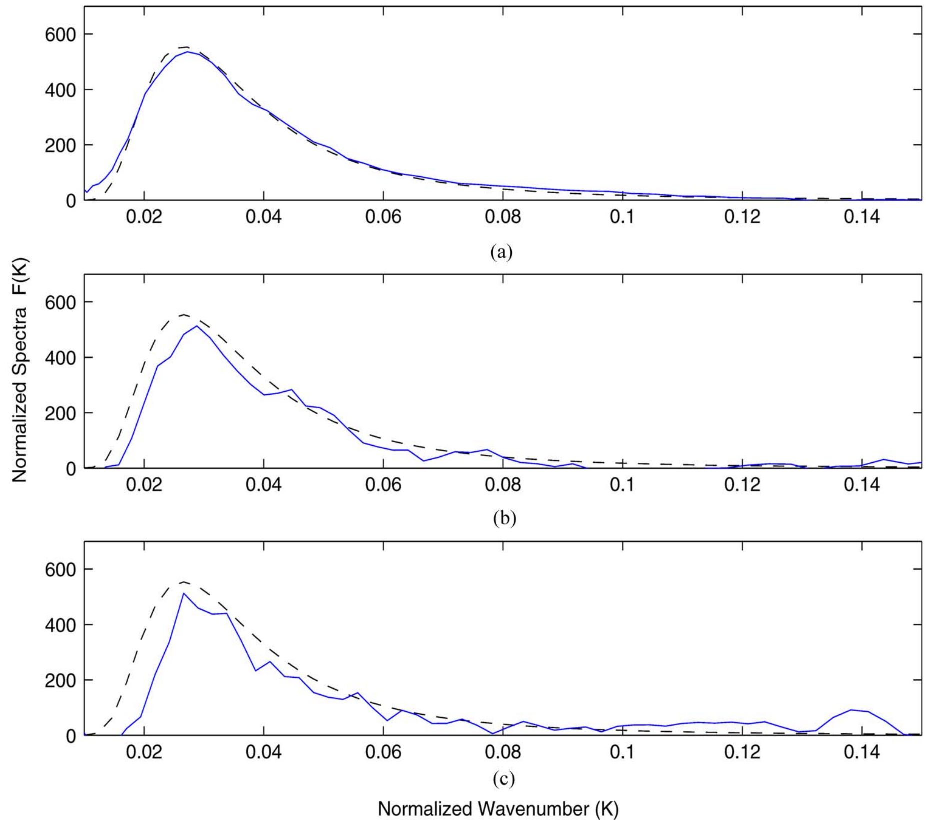

Fig. 16. Recovered nondirectional spectra from noisy radar Doppler PSD for water depths of (a) 100 m (deep water), (b) 10 m, and (c) 5 m.

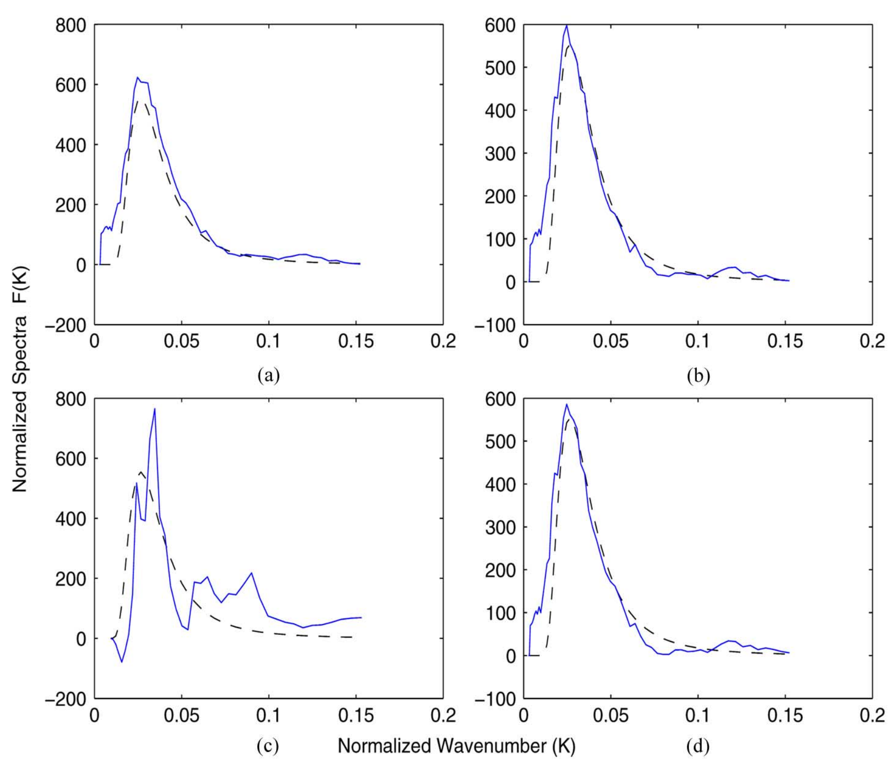

Fig. 17. Recovered nondirectional spectra from noisy radar Doppler PSD for different wind directions (wind speed: 15 m/s). Wind directions are (a) $\theta_w = 0°$, (b) $\theta_w = 45°$, (c) $\theta_w = 90°$, and (d) $\theta_w = 135°$.

free spectra. As in Section III-E, for special wave field conditions, such as lower sea state and when the wind direction is $90°$ to the x-axis, the mismatches are, not surprisingly, more significant.

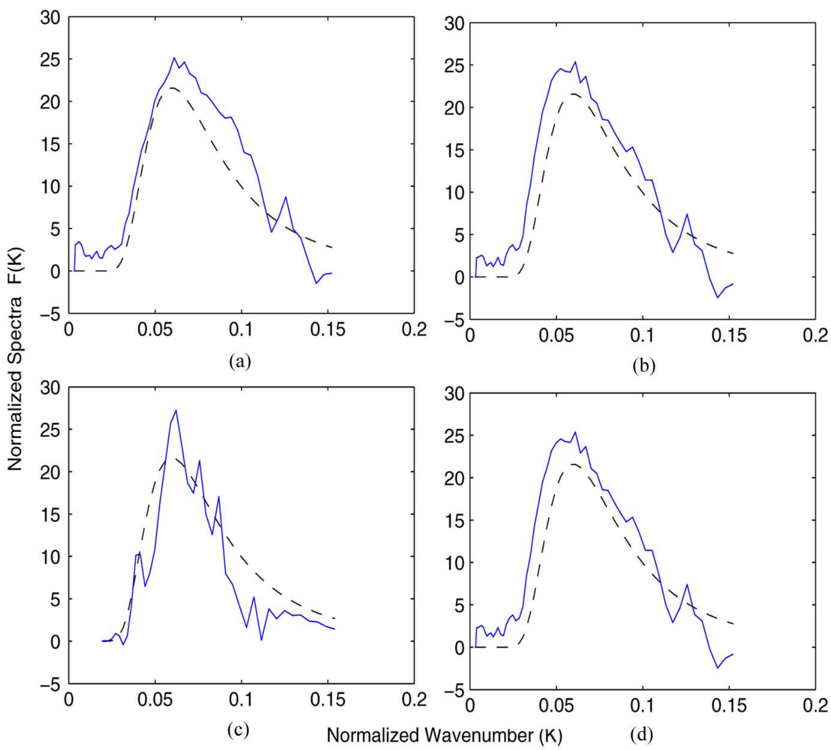

Fig. 18. Recovered nondirectional spectra from noisy radar Doppler PSD for different wind directions (wind speed: 10 m/s). Wind directions are (a) $\theta_w = 0°$, (b) $\theta_w = 45°$, (c) $\theta_w = 90°$, and (d) $\theta_w = 135°$.

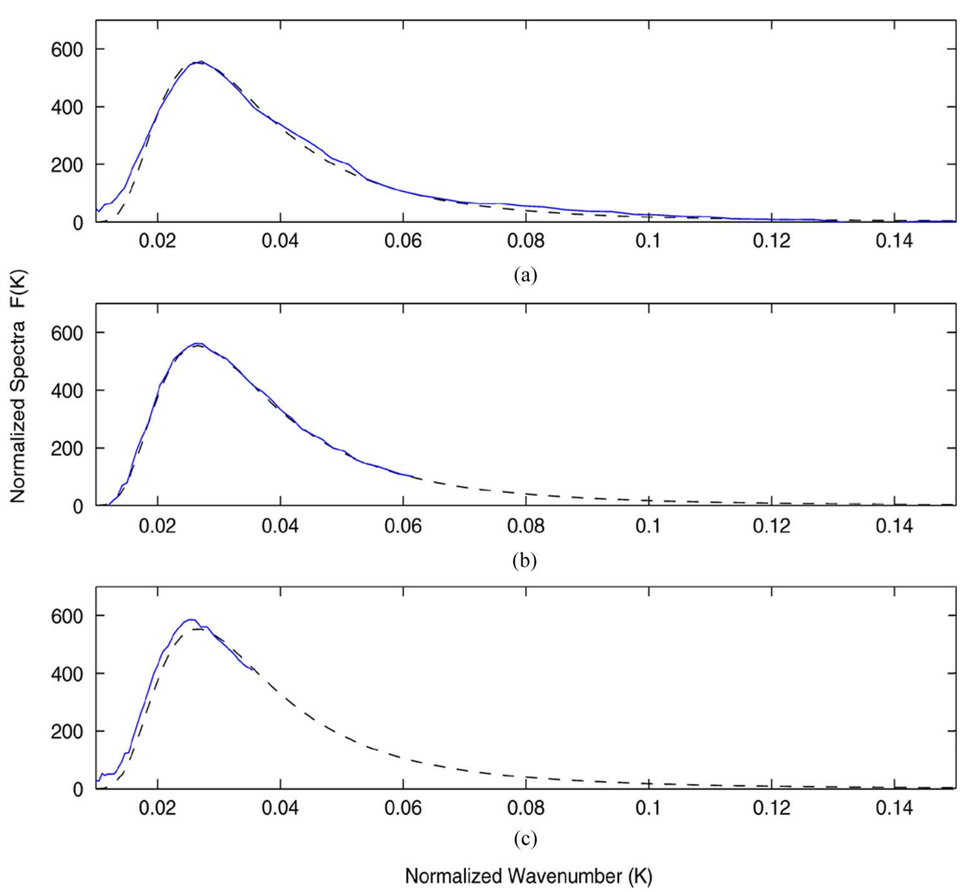

Fig. 19. Recovered nondirectional spectra from noisy radar Doppler PSD for (a) 25 MHz, (b) 10 MHz, and (c) 5.75 MHz different radar frequency.

TABLE I
COMPARISON OF NORMALIZED WAVEHEIGHTS FOR NOISE-FREE AND NOISY SPECTRA AT DIFFERENT WIND DIRECTIONS (f_0 =25 MHz, u = 10 m/s)

Directions (°)	0	45	90	135
Model	0.3289	0.3289	0.3289	0.3289
Noise-free	0.3367	0.3282	0.3527	0.3282
%Difference	2.4	0.2	7.2	0.2
Noisy	0.3549	0.3368	0.2883	0.3368
%Difference	7.9	2.4	12.3	2.4

V. CONCLUSION

Based upon bistatic cross sections developed by Gill and Walsh [17], an algorithm has been developed to derive the nondirectional ocean wave spectrum from simulated HF narrowbeam bistatic radar returns. The water depth is set to be arbitrary and the current is assumed to be absent. The inverse results for different ocean surface conditions and operating frequencies are addressed in a manner similar to that used by other investigators for the monostatic case [14]–[16].

Mathematically, the inverse scattering analysis is a problem of solving a set of Fredholm-type integral equations of the first kind. The integrand of the second-order cross-section equation contains nonlinearities resulting from the product of two related factors of ocean wave directional spectra. An approximate linearization is implemented and the path gains and losses are removed from the second-order cross section by normalizing to the first order. The discretization of the cross section is accomplished by means of a frequency band approximation. The directional ocean wave spectrum is represented by a truncated Fourier series. The original cross-section equation is then converted to a matrix equation in which the Fourier coefficients of the ocean spectrum are the unknowns. SVD is used to invert the kernel matrix of the equation. Inversion yields the ocean Fourier coefficients of which the zero-order coefficient yields the nondirectional spectrum.

While no bistatic field data were available for testing purposes, a realistic model of the Doppler PSD incorporating noise developed by Gill and Walsh [19] was used. Based upon the inverse scattering algorithm presented in Section III, nondirectional wave spectra were derived from the simulated bistatic noisy data. The results show that, even when noise is added, for the upper HF band (20–30 MHz), the linearization method works well, and most of the ocean wave spectral energy may be recovered from the bistatic HF radars data. Not surprisingly, the effect of added noise becomes increasingly significant as sea state decreases.

There is another important issue which has the possibility of affecting the results presented here, namely the problem of sidelobes in both the transmitter and receiver arrays. When sidelobes are only a few decibels below the mainbeam, it is obvious that major effects, such as spectral smearing, can be introduced into the field data. This may preclude, among other things, the determination of the position of the sea surface patch being interrogated. With the added reality of the directional nature of the sea spectrum, it is clear that a reasonable understanding of the radar beamforms is necessary in producing useful inversion results. It is proposed that these problems be considered in future analyses.

It is intended that the inversion models present here be used in the near future on bistatic data collected from HF radars installed at Cape Race and Cape Bonavista, NL, Canada. These radars have typically operated in monostatic mode only, but in the recent past the Canadian Department of National Defense has initiated experiments designed to assess the facilities of bistatic operation. While these radars are operated in the lower part of the HF band, the wave regime over the North Atlantic is such that, even at these frequencies, there will be periods when the sea state will be large enough to further test the integrity of the procedure presented here.

REFERENCES

[1] D. Crombie, "Doppler spectrum of sea echo at 13.56 mc/s," *Nature*, vol. 175, pp. 681–682, 1955.

[2] D. Barrick, "First-order theory and analysis of MF/HF/VHF scatter from the sea," *IEEE Trans. Antennas Propag.*, vol. AP–20, no. 1, pp. 2–10, Jan. 1972.

[3] D. Barrick, "Remote Sensing of the Troposphere," in *Remote Sensing of Sea State by Radar*, V. Derr, Ed.. Washington, DC: U.S. Government Printing Office, 1972, ch. 12, pp. 1–46.

[4] D. Barrick and B. Lipa, "The second-order shallow water hydrodynamic coupling coefficient in interpretation of HF radar sea echo," *IEEE J. Ocean. Eng.*, vol. OE–11, no. 2, pp. 310–315, Apr. 1986.

[5] J. Walsh, "On the theory of electromagnetic propagation across a rough surface and calculations in the VHF region" Memorial Univ. Newfoundland, St. John's, NL, Canada, OEIC Rep. N00232, 1980.

[6] S. Srivastava, "Analysis of HF scattering from an ocean surface: An alternative approach incorporating a dipole source," Ph.D. dissertation, Faculty Eng. Appl. Sci., Memorial Univ. Newfoundland, St. John's, NL, Canada, 1984.

[7] J. Walsh, R. Howell, and B. Dawe, "Model development for evaluation studies of ground wave radar" Centre for Cold Ocean Resources Eng., Memorial Univ. Newfoundland, St. John's, NL, Canada, Contract Rep. 90-C14, 1990, (Prepared for Department of National Defence, Government of Canada, DSS Contract Number W7714-8-5655/01-SS).

[8] D. Barrick, "Extraction of wave parameters from measured HF radar sea-echo Doppler spectrum," *Radio Sci.*, vol. 12, no. 3, pp. 415–424, 1977.

[9] B. Lipa, "Derivation of directional ocean-wave spectra by integral inversion of second-order radar echoes," *Radio Sci.*, vol. 12, no. 3, pp. 425–434, 1977.

[10] O. Phillips, *The Dynamics of the Upper Ocean*. Cambridge, U.K.: Cambridge Univ. Press, 1977.

[11] B. Lipa and D. Barrick, "Analysis methods for narrow-beam high-frequency radar sea echo" National Oceanic and Atmospheric Administration (NOAA), U.S. Dept. Commerce, Washington, D.C., Tech. Rep. ERL420-WPL 56, 1982.

[12] L. R. Wyatt, "The measurement of the ocean wave directional spectrum from HF radar Doppler spectra," *Radio Sci.*, vol. 21, no. 3, pp. 478–485, 1986.

[13] L. Wyatt, J. Venn, G. Burrows, A. Ponsford, M. Moorhead, and J. Van Heteren, "HF radar measurements of ocean wave parameters during NURWEC," *IEEE J. Ocean. Eng.*, vol. OE–21, no. 2, pp. 219–234, Apr. 1986.

[14] B. Lipa and D. Barrick, "Extraction of sea state from HF radar sea echo: Mathematical theory and modeling," *Radio Sci.*, vol. 21, no. 1, pp. 81–100, 1986.

[15] R. Howell and J. Walsh, "Measurement of ocean wave spectra using narrow beam HF radar," *IEEE J. Ocean. Eng.*, vol. 18, no. 3, pp. 296–305, Jul. 1993.

[16] E. Gill and J. Walsh, "Extraction of ocean wave parameters from HF backscatter received by a four-element array: Analysis and application," *IEEE J. Ocean. Eng.*, vol. 17, no. 4, pp. 376–386, Oct. 1992.

[17] E. Gill and J. Walsh, "High-frequency bistatic cross sections of the ocean surface," *Radio Sci.*, vol. 36, no. 06, pp. 1459–1475, 2001.
[18] E. W. Gill, "The scattering of high frequency electromagnetic radiation from the ocean surface: An analysis based on a bistatic ground wave radar configuration," Ph.D. dissertation, Memorial Univ. Newfoundland, St. John's, NL, Canada, 1999.
[19] E. Gill and J. Walsh, "A relationship between external noise and the ocean clutter models for bistatic operation of a pulsed high-frequency radar," in *Proc. IEEE Canadian Conf. Electr. Comput. Eng.*, 2001, vol. 1, pp. 153–158.
[20] E. Gill, W. Huang, and J. Walsh, "On the development of a second-order bistatic radar cross section of the ocean surface: A high-frequency result for a finite scattering patch," *IEEE J. Ocean. Eng.*, vol. 31, no. 4, pp. 740–750, Oct. 2006.
[21] J. Zhang, "An algorithm for the extraction of ocean wave information from bistatic HE ground wave radar data: A simulation," M.S. thesis, Faculty Eng. Appl. Sci., Memorial Univ. Newfoundland, St. John's, NL, Canada, 2003.
[22] B. Kinsman, *Wind Waves*. New York: Dover, 1984.
[23] W. Pierson and L. Moskowitz, "A proposed spectral form for fully developed seas based upon the similarity theory of S.A. Kitaigorodskii," *J. Geophys. Res.*, vol. 69, no. 24, pp. 5181–5190, 1964.
[24] D. Barrick, "The ocean waveheight nondirectional spectrum from inversion of the HE sea-echo Doppler spectrum," *Remote Sens. Environ.*, vol. 6, no. 3, pp. 201–227, 1977.
[25] D. Barrick and B. Lipa, "A compact transportable HE radar system for directional coastal wavefield measurements," in *Ocean Wave Climate*, M. D. Earle and A. M. , Eds. New York: Plenum, 1979, pp. 153–201.
[26] G. Stewart, *Introduction to Matrix Computations*. New York: Academic, 1973.
[27] *MAT LAB® The Language of Technical Computing-Using MATLAB*. Natick, MA: The MathWorks, Inc., 2000, Version 6.
[28] G. Strang, *Linear Algebra and Its Applications*. New York: Academic, 1976.
[29] J. Atanga and L. Wyatt, "Comparison of inversion algorithms for HE radar wave measurements," *IEEE J. Ocean. Eng.*, vol. 22, no. 4, pp. 593–603, Oct. 1997.
[30] Y. Hisaki, "Nonlinear inversion of the integral equal to estimate ocean wave spectra from HE radar," *Radio Sci.*, vol. 31, no. 1, pp. 25–39, 1996.

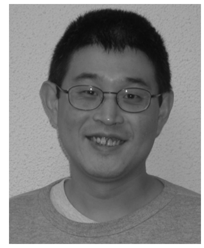

Jianjun Zhang received the B.S. and M.S. degrees in electrical engineering from Beijing University of Posts and Telecommunications (BUPT), Beijing, China, in 1989 and Memorial University of Newfoundland (MUN), St. John's, NL, Canada, in 2003, respectively. Currently, he is working towards the Ph.D. degree in electrical engineering at MUN.

From 1989 to 1999, he was an Electrical Engineer at State Radio Monitoring Centre, Ministry of Information Industry (MII), Beijing, China. His present research interests include remote sensing of ocean surface wave and current information by HF radar.

Eric W. Gill (M'00–SM'05) received the B.Sc. degree in physics and the M.Eng. and Ph.D. degrees in electrical engineering from Memorial University of Newfoundland (MUN), St. John's, NL, Canada, in 1977, 1990, and 1999, respectively.

In 1977, he was a Lecturer in Physics at the College of the North Atlantic (formerly, Cabot Institute of Applied Arts and Technology). Since 2000, he has been teaching and conducting research in theoretical and applied electromagnetics in the Faculty of Engineering and Applied Science, MUN. His interest is in the scattering of HF electromagnetic radiation from time-varying, randomly rough surfaces, with particular application to the use of ground wave radar in remote sensing of the marine environment.

Dr. Gill is a member of the American Geophysical Union.